Frustrated magnetism in Mn films on Ag(111) surface: From chiral in-plane Néel state to row-wise antiferromagnetism

Selcuk Sözeri,[1,2] Nihad Abuawwad,[1,2] Amal Aldarawsheh,[1,2] and Samir Lounis[1,2,3]
[1]*Faculty of Physics, University of Duisburg-Essen and CENIDE, 47053 Duisburg, Germany*
[2]*Peter Grünberg Institut, Forschungszentrum Jülich and JARA, 52425 Jülich, Germany*
[3]*Institute of Physics and Halle–Berlin–Regensburg Cluster of Excellence CCE, Martin Luther University Halle-Wittenberg, 06099 Halle, Germany*

(Received 19 December 2024; accepted 15 December 2025; published 10 March 2026)

We conduct a comprehensive density functional theory study to explore the intricate magnetic properties of frustrated Mn monolayer on the Ag(111) surface. Spin-polarized scanning tunneling microscopy demonstrates that a Néel magnetic state characterizes such an interface, which contradicts systematic *ab initio* predictions made in the last two decades indicating that the ground state is collinear row-wise antiferromagnetic (RW-AFM) state. Here, we employ the all-electron full-potential Korringa-Kohn-Rostoker Green's function method and find that the ground state is a chiral magnetic Néel state, with magnetic moments rotating in the surface plane following a unique sense of rotation, as dictated by the underlying in-plane magnetic anisotropy and Dzyaloshinskii-Moriya interaction. Changing the stacking of the Mn monolayer from fcc to hcp switches the chiral nature of the Néel state. Once allowing disordered magnetic states, as described within the disordered local moment approach, we reveal the possibility of stabilization of a RW-AFM state. We conjecture that at low temperatures, the chiral Néel state prevails, while at higher temperatures, the magnetic exchange interactions are modified by magnetic disorder, which can then induce a transition towards a RW-AFM state. Our work addresses a long-term experimental-theoretical controversy and provides significant insights into the magnetic interactions and stability of Mn films on noble metal substrates, contributing to the broader understanding of the different magnetic facets of frustrated magnetism in thin films.

DOI: 10.1103/twpb-shbv

I. INTRODUCTION

Frustrated magnets, where competing interactions between neighboring spins cannot be simultaneously satisfied, give rise to complex and intriguing phenomena. This frustration creates a highly degenerate ground state and lies at the heart of noncollinear antiferromagnetism, giving rise to exciting properties such as Hall effects [1], torques [2], and topological spin textures [3–5]. A classic example is a two-dimensional hexagonal lattice of antiferromagnetic atoms, where the topological constraints make it impossible to align all neighboring spins in an antiparallel arrangement. In certain conditions, frustration can lead to the formation of spin liquid states, exhibiting remarkable collective behaviors, in which spins remain highly correlated but continue to fluctuate, even at absolute zero [6]. The study of these frustrated spin structures is not only fundamental to understanding exotic magnetic states but also critical for advancing spintronics applications [7].

The exploration of magnetic frustration in the limit of two-dimensional materials has been pursued for decades. A two-dimensional hexagonal (or triangular) arrangement of antiferromagnetic atoms is typically achieved by depositing a single monolayer (ML) of magnetic elements, expected to be antiferromagnetic such as manganese (Mn), onto hexagonal surfaces initially nonmagnetic, e.g., (111) surfaces of fcc crystals. For instance, a Mn ML on Ag(111) surface has been the subject of extensive study over the years, encompassing both theoretical and experimental approaches. Intuitively and due to magnetic frustration induced by nearest-neighboring (NN) antiferromagnetic (AFM) interactions, a 120° Néel state is anticipated as the ground state [see the comparison illustrated in Fig. 1 between a Néel state and a row-wise antiferromagnetic (RW-AFM) configuration]. In the former, the NN magnetic moments are rotated by an angle of 120°. However, early first-principles investigations [8,9] based on the Full-potential Linearized Augmented Plane Wave method predicted a different ground state for Mn/Ag(111): a RW-AFM state [Fig. 1(a)]. The latter was consistently supported by subsequent studies employing various *ab initio* methods based on density functional theory (DFT). Notable examples include the use of pseudopotentials [10], tight-binding linear muffin-tin orbitals [11], and the all-electron Korringa-Kohn-Rostoker (KKR) Green's function formalism in the atomic sphere approximation [12].

Despite the consistency of these theoretical findings, state-of-the-art spin-polarized scanning tunneling spectroscopy measurements undoubtedly indicate that a Mn ML grown on Ag(111) hosts a Néel magnetic state [13]. This long-standing discrepancy between theoretical predictions and experimental observations, persisting for several decades, presents an

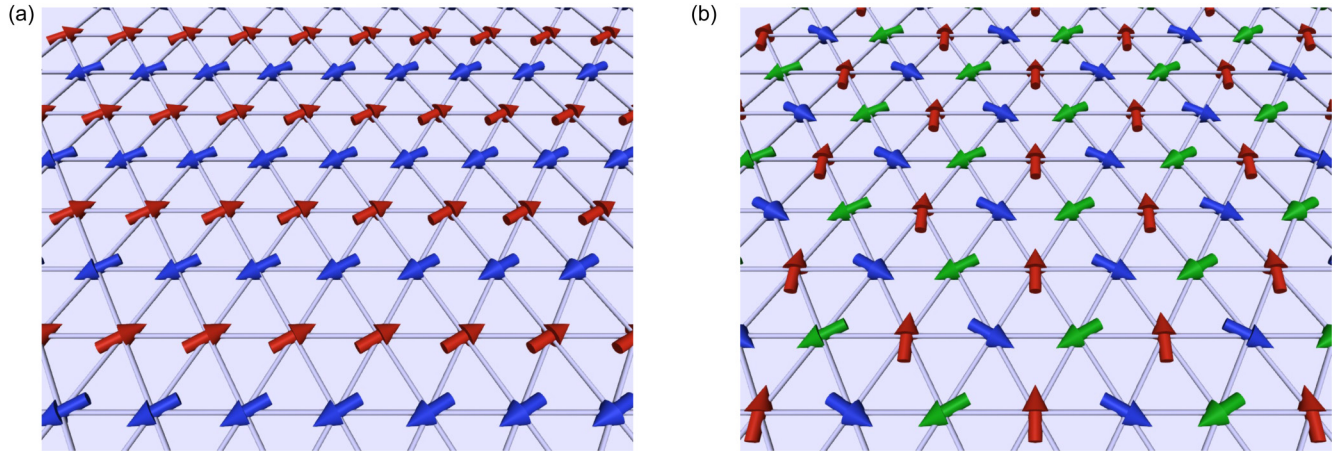

FIG. 1. (a) Illustration of a row-wise antiferromagnetic (RW-AFM) state on a triangular lattice, where adjacent rows exhibit alternating spin orientations. (b) Illustration of a Néel state on a triangular lattice, characterized by a spin arrangement where neighboring spins are aligned in a noncollinear configuration with a rotation angle of 120°, minimizing frustration in the triangular geometry.

intriguing puzzle and underscores the complexities of modeling such systems. More recently, the Néel state of a Mn monolayer has been observed on a different substrate, the Ir(111) surface [14], which as predicted theoretically can host frustrated topological spin textures [3].

In this paper, we aim to address the persistent issue in describing the magnetic ground state of a Mn ML on Ag(111). We compare our findings to previous studies and discuss the decisive mechanisms for the emergence of the Néel state. While we recover the measured magnetic state utilizing the all-electron full-potential KKR method, we demonstrate the chiral nature of the Néel state and explore the impact of magnetic disorder within the disordered local moment (DLM) approach. The latter enables one to mimic the impact of temperature, and shows that the RW-AFM state can be recovered if disorder is incorporated.

II. METHODS

A. First-principles calculations

We use a combination of *ab initio* methods based on DFT to explore the magnetic behavior of Mn monolayer on Ag(111) surface.

We start by assessing the interlayer atomic distances by employing the projector augmented-wave pseudopotential method [15], as implemented in the quantum espresso) package [16], which is efficient to treat atomic relaxations. We employed a slab geometry consisting of five layers of Ag atoms and one additional Mn overlayer. Each atomic layer contains one atom, corresponding to a 1×1 hexagonal surface unit cell. A vacuum region of approximately 13.6 Å (equivalent to roughly four Ag layers) was added along the surface normal to prevent interactions between periodic images.

We assumed a k-mesh resolution of $20\times20\times1$, while the plane-wave and energy cutoffs are considered to be 110 Ry and the convergence criterion for the total energy is set to 0.01 μRy. During the relaxation process, the atomic positions were optimized to ensure that the residual forces on the atoms were less than 1 mRy a_0^{-1}.

Once the geometry is optimized, we explore the magnetic properties adopting the DFT-based all-electron full-potential KKR method, utilizing the jukkr code [17] where spin-orbit coupling is included self-consistently. The method enables the exploration of noncollinear structures as well as the inclusion of the coherent potential approximation (CPA), which permits the investigation of magnetic disorder in the so-called DLM approach [18–20]. DLM describes how the electronic structure responds to thermal fluctuations of the local moments. The Mn layer is then assumed to be an alloy $\mathrm{Mn}_p\mathrm{Mn}_{1-p}$ made of magnetic moments pointing either in one ↑ or the opposite direction ↓, with $p = 50\%$ being the paramagnetic state expected at high temperatures. We treated the exchange-correlation interactions with the local density approximation, as formulated by Vosko *et al*. [21].

In the KKR calculations, the surface was modeled as a finite slab consisting of five layers of Ag atoms and one Mn layer adsorbed on one side. The slab is embedded in vacuum, with a thickness equivalent to four Ag layers on each side. Similarly to the pseudopotential method, we employed a k-points grid mesh of $20\times20\times1$ for the self-consistent calculations. The angular momentum expansion of the Green's function was truncated at $l_{\max} = 3$, and energy integration was performed along the complex plane including a Fermi-Dirac smearing of 502.78 K. To extract the exchange interaction parameters such as the Heisenberg exchange and the Dzyaloshinskii-Moriya interaction (DMI) [22,23], we used the infinitesimal rotation method [24,25] starting from the ferromagnetic reference configuration in the case of an ordered state (see Appendix A for a succinct description) with a finer k-points grid mesh of $200\times200\times1$ and a Fermi-Dirac smearing of 502.78 and 200 K. The magnetic interactions were found unaffected by the different explored temperatures. This approach was also applied within the DLM framework (see Appendix B), ensuring methodological consistency between the ordered and disordered magnetic configurations [26–28].

B. Magnetic interactions and atomistic spin dynamics

The magnetic interactions obtained from the first-principles calculations are used to parametrize the following

classical extended Heisenberg Hamiltonian (see Appendix A):

$$H = -\sum_{i,j} \mathbf{S}_i \cdot \mathcal{J}_{ij} \cdot \mathbf{S}_j - \sum_i K_i (S_i)^2 = -\sum_{i,j} J_{ij} \mathbf{S}_i \cdot \mathbf{S}_j - \sum_{i,j} \mathbf{D}_{ij} \cdot (\mathbf{S}_i \times \mathbf{S}_j) - \sum_i K_i \left(S_i^z\right)^2. \quad (1)$$

Here i and j label different magnetic sites carrying a magnetic moment, whose orientation is defined by the unit vector $\mathbf{S}$, while $\mathcal{J}$ denotes the exchange interaction tensor.

The tensor elements can be decomposed into the isotropic Heisenberg exchange coupling J and the DMI vector $\mathbf{D}$.

The symmetric anisotropic contribution, which is quadratic in spin-orbit coupling, has not been considered in the previous equations since it is found negligible from our *ab initio* simulations. The positive sign of the magnetic anisotropy energy K indicates a preference for an out-of-plane orientation of the moments.

After extraction of the magnetic interactions, a Fourier transformation is performed: $\mathcal{J}_{ij}(\mathbf{q}) = \sum_j \mathcal{J}_{0j} e^{-i\mathbf{q}\cdot\mathbf{R}_{0j}}$, where $\mathbf{R}_{0j}$ is a vector connecting unit cells atom 0 and j.

By evaluating the associated eigenvalues, one obtains the dispersion curves of spin spirals characterized by the wave vector $\mathbf{q}$.

Furthermore, atomistic spin dynamic simulations using the Landau-Lifshitz-Gilbert equation equation as implemented in the spirit code [29,30] are performed in order to explore the existence and stability of various trivial and complex magnetic states. Once the magnetic ground state was identified using the atomistic spin model, the stability of the spin texture has been once more studied via DFT.

III. RESULTS AND DISCUSSION

A. Atomic relaxations

We examine two possible stacking configurations for the Mn ML on the Ag(111) surface: fcc and hcp. Upon structural relaxation, the Mn layer shifts inward toward the Ag substrate by 2.48% (fcc) and 2.29% (hcp) relative to the ideal Ag interlayer distance. This inward relaxation of the Mn ML is accompanied by a moderate outward relaxation of the topmost Ag layers: the spacing between the surface and subsurface Ag layers increases by 3.39% for fcc stacking and 3.74% for hcp stacking, again with respect to the ideal bulk spacing. Comparing the two configurations, we find that the fcc stacking is energetically more favorable than the hcp one, with an energy difference of 6.83 meV.

B. Heisenberg exchange interactions

We now turn our attention to the analysis of the magnetic exchange interactions as a function of interatomic distances, illustrated in Fig. 2(a). Specifically, we investigate two scenarios: first, a freestanding hexagonal Mn ML with the Ag lattice parameter imposed (as done previously in Refs. [8,9]), and second, a configuration in which the Mn layer is supported by the Ag(111) substrate, assuming an fcc stacking. Figure 2(a) clearly reveals the presence of significant antiferromagnetic Heisenberg exchange interactions extending up to the fourth-nearest neighbors. At larger distances, the interactions exhibit an oscillatory behavior, as expected for Ruderman-Kittel-Kasuya-Yosida interactions in metallic systems. The figure unambiguously demonstrates that hybridization with the substrate strongly affects the Heisenberg exchange interactions.

Notably, the exchange interactions involving the first-, second-, and third-nearest neighbors are markedly reduced when manganese is interfaced with silver. As will be shown later, this reduction plays a crucial role in driving the transition of the system's ground state from one magnetic configuration to a completely different one. Interestingly, this reduction follows a nearly identical trend for both fcc- and hcp-stacked Mn layers on Ag(111), suggesting that the stacking sequence has only a minor influence on the magnetic exchange parameters. This observation is further supported by comparing the local density of states (LDOS) and exchange interactions for both stacking types [see Figs. 3(a) and 3(b)].

Equipped with the exchange parameters, we can now explore the magnetic ground state dictated by the full exchange tensor. This can be investigated by analyzing the eigenvalues of the Fourier-transformed exchange matrix, as illustrated in Fig. 2(c) for the fcc stacking. The minimum is located at the K point, which corresponds to the Néel magnetic state—consistent with spin-polarized scanning tunneling microscopy (SP-STM) measurements reported by Gao *et al.* [13]. Although this represents the ground state, the dispersion exhibits a rather flat energy landscape in the surrounding region, indicating the presence of energetically close metastable spin-spiral states of antiferromagnetic nature. Note that Fig. 2(c) shows two dispersion curves corresponding to spin spirals propagating along opposite high-symmetry directions in the Brillouin zone. The observed asymmetry is a consequence of the DMI, which is discussed in the next subsection. For the fcc stacking, the energy difference between the minimum and the RW-AFM configuration amounts to 27.5 meV.

In contrast, for the hcp-stacked Mn layer on Ag(111), the minimum is shifted to the $-K$ point of the Brillouin zone, as shown in Fig. 3(c). This subtle change indicates a different preferred propagation direction of the spin spiral. The associated energy difference between the Néel and RW-AFM states is slightly smaller in this case, amounting to -26.3 meV. These findings underline that while the stacking sequence (fcc vs hcp) has a minor impact on the overall magnetic interaction strength (as reflected in similar LDOS and exchange parameters), it can influence the detailed symmetry and directionality of the magnetic ground state.

To further interpret these results, it is instructive to examine the phase diagram of an antiferromagnetic hexagonal monolayer by considering up to third-nearest-neighbor interactions, in line with previous work [8,9]. This is a simplified model in that we cut out the long-range magnetic interactions obtained from DFT. Assuming an antiferromagnetic first-nearest-neighbor exchange interaction J_1, we obtain the phase diagram shown in Fig. 4. One can observe that for sufficiently strong ferromagnetic second (J_2) and third (J_3) nearest-neighbor interactions, the system adopts a ferromagnetic ground state despite the antiferromagnetic J_1. Upon decreasing J_2 while keeping J_3 ferromagnetic, the system transitions into the RW-AFM phase, which has also been

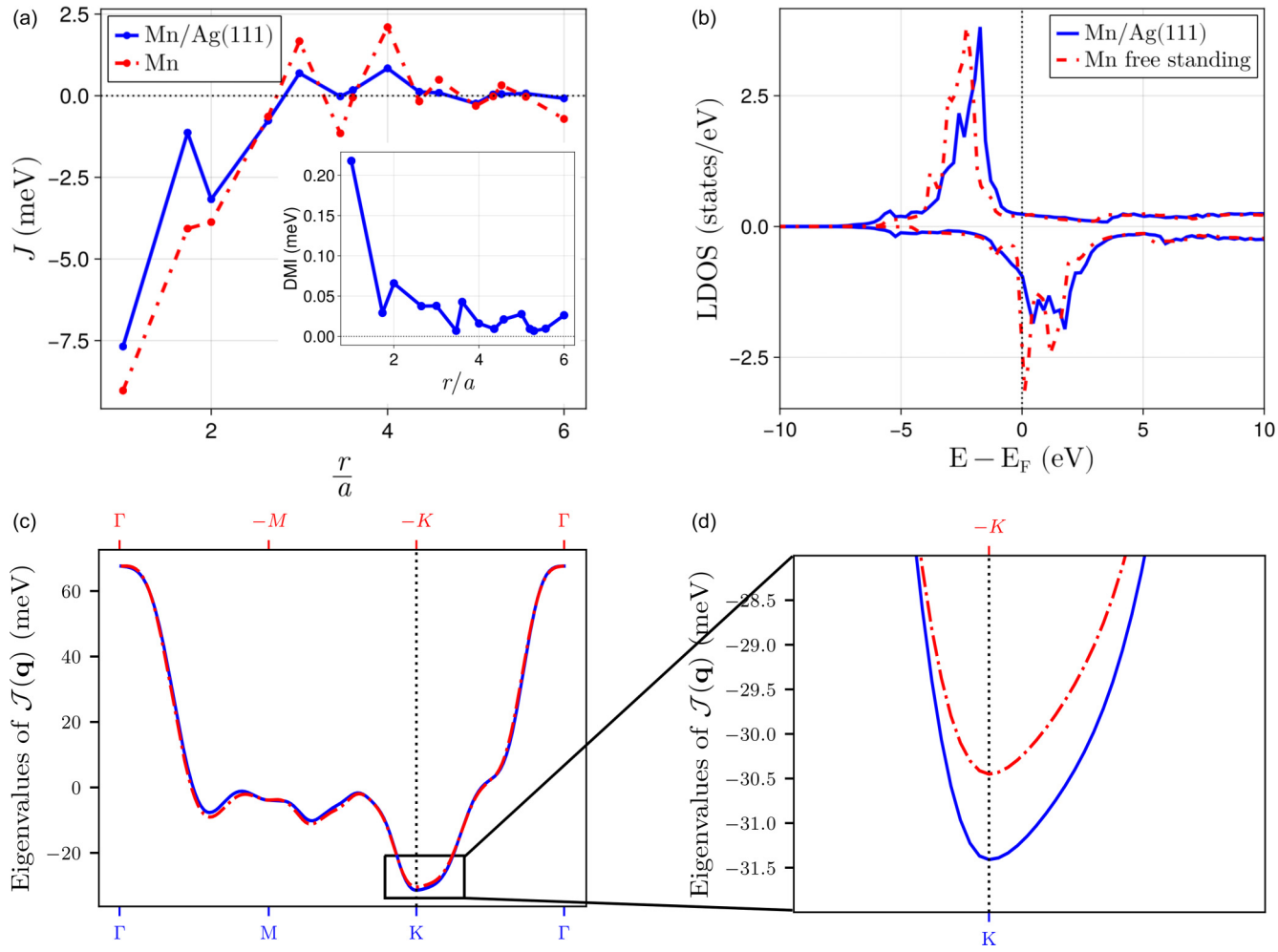

FIG. 2. (a) The Heisenberg exchange interactions as a function of distance for Mn/Ag(111) (blue) and the unsupported Monolayer Mn (red) while the inset shows the DMIs. (b) Spin-resolved local density of states (LDOS) of Mn/Ag(111) (blue) and Mn (red). (c) Eigenvalues of the Fourier-transformed tensor of exchange interactions high-symmetry paths for Mn/Ag(111). The lowest values indicate the ground state. The DMI-induced split blue and red curves in (c) correspond to spin spirals along opposite high-symmetry directions. (d) Zoom-in of the low-energy region of (c) along the relevant high-symmetry path, highlighting the DMI-induced splitting of the lowest eigenvalues.

observed experimentally by SP-STM in fcc-stacked Mn on Re(0001) [31].

Interestingly, a similar magnetic state has been predicted for a Cr monolayer interfaced with a PdFe bilayer grown on Ir(111) [32]. Reversing the sign of J_3 induces a transition to a spin-spiral antiferromagnetic state. Further reducing J_2 stabilizes the Néel state. Based on the exchange parameters obtained from our simulations, and considering interactions up to third-nearest neighbors, we find that the Néel state is the ground state for Mn on Ag(111) for both the fcc- and the hcp-stacked Mn.

Removing the Ag(111) substrate leads to an increase in the relative strength of J_2 compared to J_3, thereby stabilizing the antiferromagnetic spin-spiral phase close to the phase boundary with the Néel state. This behavior can be attributed to substrate-induced changes in the electronic structure, as shown in Fig. 2(b). In the absence of the substrate, the exchange splitting increases, leading to enhanced magnetic moments and stronger effective nearest-neighbor couplings, while the interaction between second-nearest neighbors becomes relatively weaker. Utilizing previously published data [8,9], we confirm that the magnetic ground state shifts from the RW-AFM configuration to a spin-spiral state near the RW-AFM boundary when considering exchange interactions up to the third-nearest neighbors (see Fig. 4).

C. Impact of spin-orbit coupling and spin chirality

The magnetic anisotropy energy (MAE) favors an in-plane orientation of the magnetic moments for both stacking configurations. The calculated MAE amounts to −0.13 meV. In addition to the MAE, spin-orbit coupling from the Ag(111) substrate induces a substantial DMI, as depicted in the insets of Figs. 2(a) and 3(a).

For the fcc stacking, the DMI vectors, which mediate chiral interactions between nearest neighbors, rotate in a clockwise fashion [see Fig. 5(c)], with a magnitude of approximately 0.22 meV. This chiral interaction stabilizes a Néel-type spin configuration, shown in Fig. (5). It is energetically favored over its counterpart displayed in Fig. 5(b) by 0.95 meV. The latter state is constructed by reversing the sign of the z component of the DMI vectors [cf. Fig. 5(d)], which effectively switches the chirality of the spin configuration—altering the

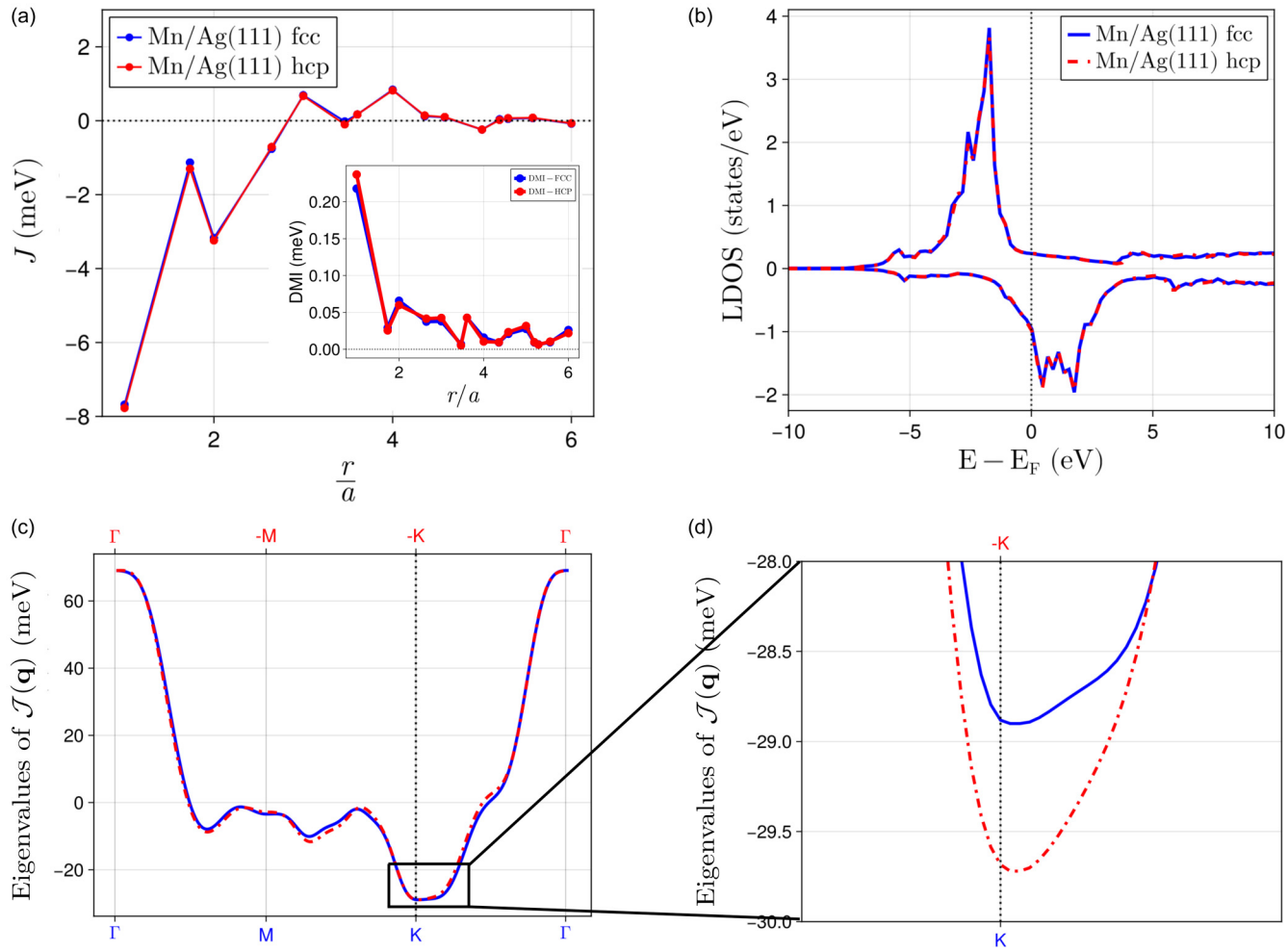

FIG. 3. (a) The Heisenberg exchange interactions as a function of distance for the fcc-Mn/Ag(111) (blue) and the hcp-Mn/Ag(111) (red) while the inset shows the DM interactions. (b) Spin-resolved local density of states (LDOS) of fcc-Mn/Ag(111) (blue) and hcp-Mn/Ag(111) (red). (c) Eigenvalues of the Fourier-transformed tensor of exchange interactions high-symmetry paths for Mn/Ag(111). The lowest values indicate the ground state. The DMI-induced split blue and red curves in (c) correspond to spin spirals along opposite high-symmetry directions. (d) Zoom-in of the low-energy region of (c) along the relevant high-symmetry path, highlighting the DMI-induced splitting of the lowest eigenvalues.

orientation of two spins within the trimer motifs highlighted in Figs. 5(a) and 5(b). Dark- (light-) blue DMI vectors in Figs. 5(c) and 5(d) indicate a negative (positive) z component of the DMI vector. One notices that Fig. 5(d) can be recovered from Fig. 5(c) by rotating the pair of atoms by $\frac{\pi}{3}$ with respect to the central one.

The impact of chiral interactions is also apparent in Fig. 2(c), where the degeneracy of the eigenvalues of the Fourier-transformed exchange tensor $\mathcal{J}(\mathbf{q})$ is lifted. This is observed when plotting the eigenvalues along opposite high-symmetry directions in the Brillouin zone:

$$\Gamma \to M \to K \to \Gamma \quad \text{versus} \quad \Gamma \to -M \to -K \to \Gamma.$$

The energy difference between the two chiral Néel states is consistently reproduced using both the SPIRIT simulations and the eigenvalue spectra of $\mathcal{J}(\mathbf{q})$, confirming the reliability of the results. According to our simulations, Mn/Ag(111) in fcc stacking hosts a chiral Néel ground state with in-plane rotating moments, as depicted in Fig. 5(a).

Turning to the hcp stacking, the spin configuration illustrated in Fig. 5(b) becomes surprisingly the magnetic ground state, while the configuration shown in Fig. 5(a) is now the higher-energy chiral counterpart. This inversion of chiral preference highlights the sensitivity of the magnetic ground state to the detailed stacking arrangement, despite the similarity in the overall interaction strengths. Indeed, the DMI values—shown in Fig. 3(a)—are found to be nearly identical to those of the fcc configuration, with a slight enhancement of the hcp NN DMI. The sign of the D_z component switches, however, when changing the stacking while the D_x and D_y components remain nearly unaffected.

Since the DMI is induced by the Ag surface atoms, this behavior can be attributed to the stacking-dependent geometrical chirality of Mn-Ag-Mn triangles, formed by two neighboring Mn atoms sharing a common nearest-neighboring Ag atom. This chirality, $\boldsymbol{\chi}$, which dictates the direction of the DMI vector according to the Fert-Lévy model [33] (although derived for large separations) is defined as $\boldsymbol{\chi} = \mathbf{e}_{\text{Ag-Mn}_1} \times \mathbf{e}_{\text{Ag-Mn}_2}$, with $\mathbf{e}$ denoting unit vectors from the Ag atom to each Mn

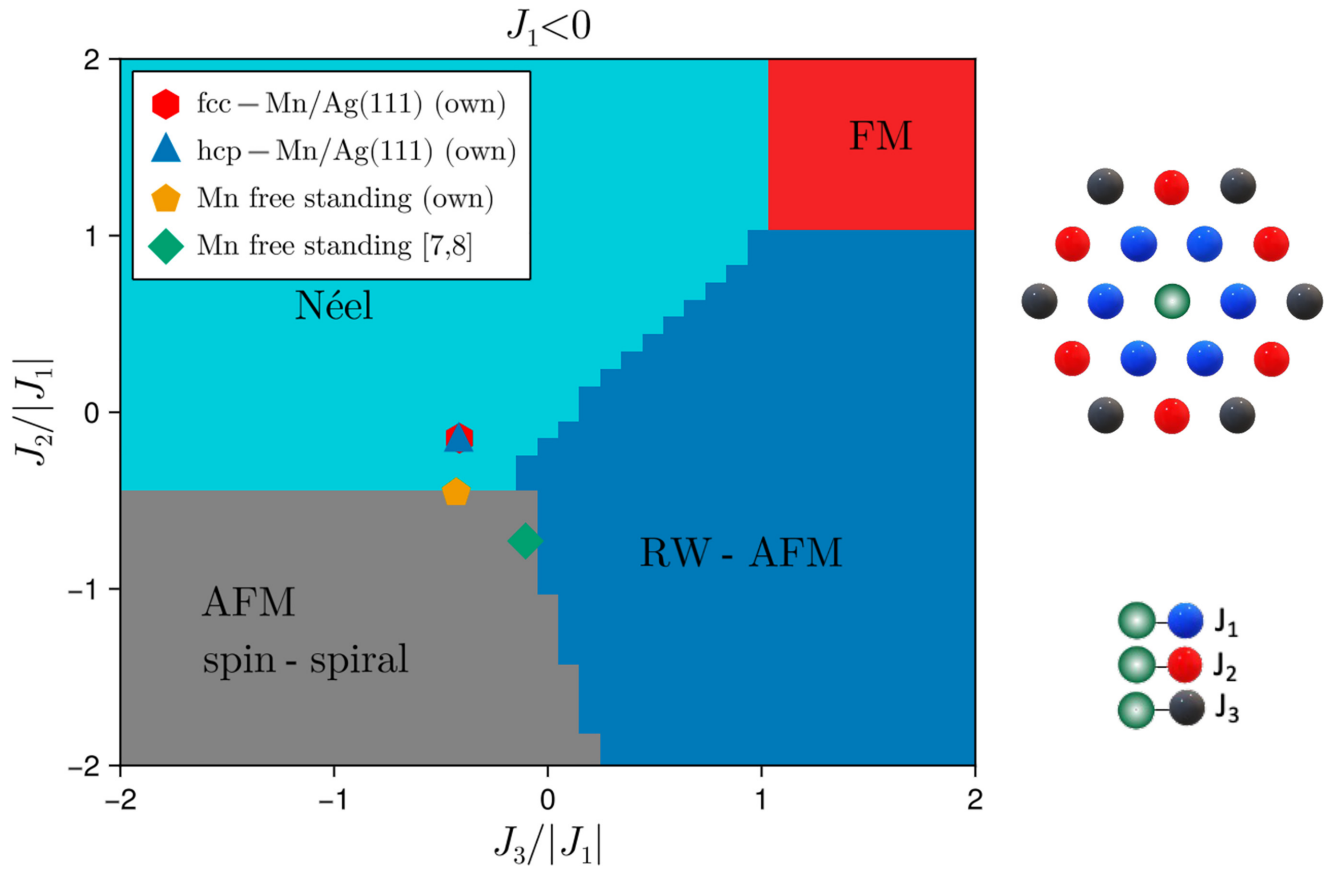

FIG. 4. Phase diagram for the Heisenberg model on a triangular lattice without spin-orbit-induced interactions, considering magnetic exchange interactions up to the third-nearest neighbors. The interactions are illustrated on the right-hand side for a two-dimensional hexagonal lattice. J_1 (assumed antiferromagnetic), J_2, and J_3 are the interactions between the central atom and the first (blue), second (red), and third (black) NN atoms, respectively. Four phases emerge: ferromagnetic (FM), RW-AFM, Néel, and AFM spin spirals. Our simulations locate the ground state for Mn/Ag(111) in the Néel sector while the Mn freestanding case hosts AFM spin spirals. The result of previous simulations [8,9] when limited to the three/new NN interactions is also indicated.

atom. As seen in Figs. 5(e) and 5(f), the fcc and hcp stacking geometries, considering only the Mn monolayer and top Ag layer, are related by a $\frac{\pi}{3}$ rotation, resulting in the DMI vector pattern shown in Fig. 5(d). As an example, for Mn pairs along the x direction, the change of stacking mirrors the Ag atom across the xz plane containing the Mn pair, thereby reversing the sign of χ_z while maintaining the in-plane components.

D. Energy differences from full *ab initio* simulations

In the previous sections, we used the tensor of magnetic exchange interactions and the MAE extracted from *ab initio* to explore the magnetic ground state. We identified the chiral in-plane Néel magnetic state to be the ground state. For completeness, it is important to check whether this behavior is confirmed by full *ab initio* simulations, where we impose the different chiral in-plane Néel magnetic states and compare the total energies to that of the RW-AFM state.

This requires the use of a supercell that is larger than the one assumed for the extraction of the magnetic exchange interactions. We employed a 3×2 surface supercell in the lateral directions, each atomic layer containing six atoms, with a slab thickness similar to what we used previously.

Assuming a temperature of 200 K, identical to that used for extracting the magnetic interactions, we find an energy difference of 17.44 and 19.49 meV/Mn for the fcc- and hcp-stacked Mn monolayers, respectively, between the chiral in-plane Néel and the RW-AFM magnetic states. These values are in qualitative agreement with the energy differences obtained from the atomistic spin model, which yield 27.50 meV/Mn for the fcc and 26.30 meV/Mn for the hcp stacking. In addition, the DFT calculations show that reversing the chirality of the in-plane Néel state requires 0.50 meV/Mn for the fcc and 0.91 meV/Mn for the hcp stacking, in excellent agreement with the results of the spirit simulations.

E. Disordered local moment approximation

Next, we examine the influence of temperature on the exchange interaction within the DLM framework briefly described in Appendix B [18–20,34]. Increasing temperature induces spin fluctuations that gradually disrupt the long-range magnetic order and reduce the overall spin polarization of the system's electronic structure. As described in the method section, magnetic disorder is modeled via the concentration of magnetic moments pointing in either direction on each Mn site. Figures 6(a) and 7(a) show the evolution of the Heisenberg exchange interactions with increasing magnetic disorder

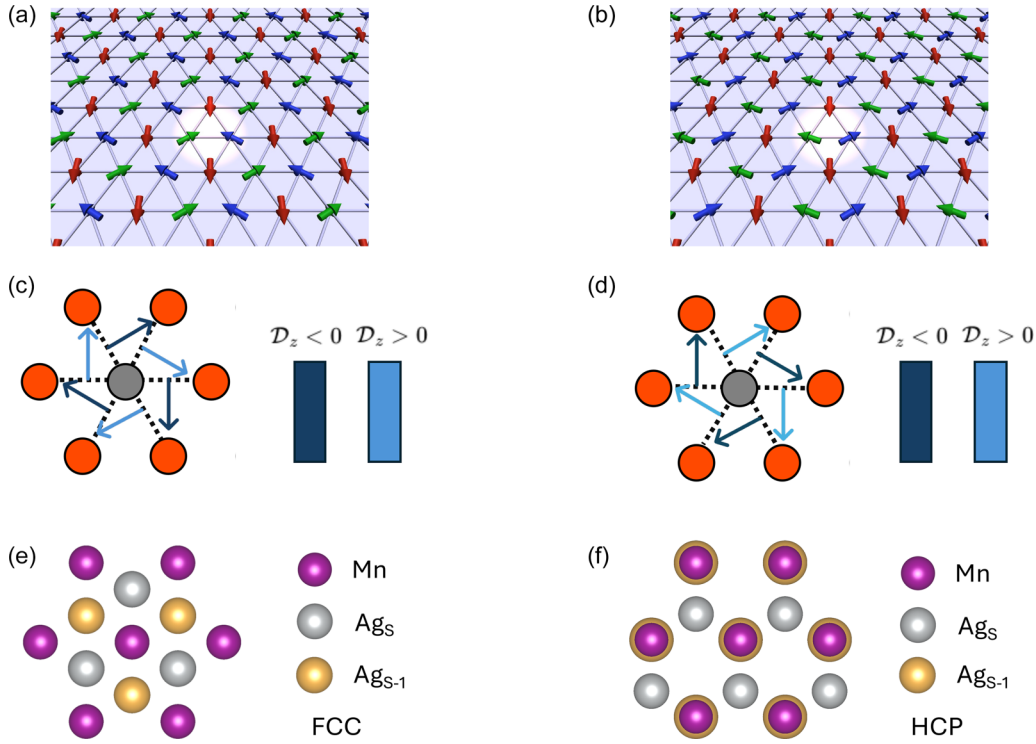

FIG. 5. In-plane Néel states of different chiral nature. (a) The ground states dictated by the DMI vectors as obtained from our DFT simulations. The NN DMI vectors rotate clockwise as shown in (c). (b) The chiral nature of the Néel state changes when flipping the sign of the z component of the DMI vector [shown in (d)], where dark blue denotes $D_z < 0$ and light blue denotes $D_z > 0$. The latter component enforces a rotation of the moments within the surface plane, with its sign determining the direction of the rotation. The highlighted trimers in (a) and (b) clearly show the distinct nature of their respective chiral states. The red magnetic moment is fixed, while the other ones have their directions switched. Atomic stacking geometries at the Mn/Ag(111) interface for the (e) fcc stacking and (f) hcp stacking. To highlight the different vertical registries of the substrate, the Ag layer (Ag_{S-1}) beneath the interfacial Ag layer (Ag_S) is also shown. The DMI between the Mn atoms is mainly mediated by the Ag atoms of the Ag_S layer. Considering only the two layers, Mn and Ag_S, the two geometries are related by an in-plane rotation of the Ag_S layer by $\frac{\pi}{3}$ while keeping the Mn layer fixed. This change alters the geometrical chirality χ of the Mn-Ag-Mn triangles, which governs the direction of the Dzyaloshinskii-Moriya interaction vectors according to the Fert-Lévy model [33].

for fcc- and hcp-stacked Mn/Ag(111), respectively. The concentration varies from 50% (paramagnetic limit) to 100% (fully ordered), in steps of 10%. Here, 50% corresponds to an equal mixture of moments pointing up or down on each site.

The data reveal qualitatively similar trends for both stacking types. While the nearest-neighbor Heisenberg and DMI interactions remain nearly constant across the disorder range, the second- and third-nearest-neighbor interactions change significantly: J_2 increases with disorder, whereas J_3 decreases and even reverses sign below 70% magnetic order. This modifies the magnetic ground state, shifting it from a chiral Néel state towards a collinear RW-AFM phase, as summarized in the phase diagrams in Figs. 6(b) and 7(b) based on the simplified Heisenberg model limited to three NN interactions.

Notably, the MAE is strongly suppressed even by small amounts of disorder, indicating that the in-plane orientation of the moments is not preserved at elevated temperatures, despite stable spin moments.

The eigenvalue spectra of the Fourier-transformed exchange interactions in Figs. 6(c) and 7(c) confirm this transition. For disorder concentrations between 50% and 80%, the global minimum lies at the M point, corresponding to the RW-AFM ground state. Above 90% concentration, the minimum shifts to the K point, signaling the Néel state as the preferred ground state. The reversed path in Fig. 7(c) for the hcp stacking reflects the inverted symmetry compared to the fcc case, yet the qualitative behavior of the eigenvalue evolution is nearly identical.

Furthermore, the chirality of the magnetic moments changes with disorder. For fcc stacking, the Néel state depicted in Fig. 5(a) is stable at high order, while its mirror image [Fig. 5(b)] appears at intermediate disorder. In the hcp stacking, this behavior is reversed, consistent with the sign switching of the z component of the DMI vector.

Table I lists the numerical values of exchange interactions and anisotropies for fcc and hcp stackings, respectively, corroborating these findings and highlighting the crucial role of stacking geometry in the temperature-driven evolution of the magnetic ground state.

IV. CONCLUSIONS

We performed extensive *ab initio* simulations to address the magnetic ground state of a Mn monolayer on the Ag(111) surface. This AFM material was previously predicted from *ab initio* to host a RW-AFM ground state, which was contradicted by SP-STM measurements that demonstrate a Néel magnetic state. Our work addresses a long-standing puzzle in magnetic thin films.

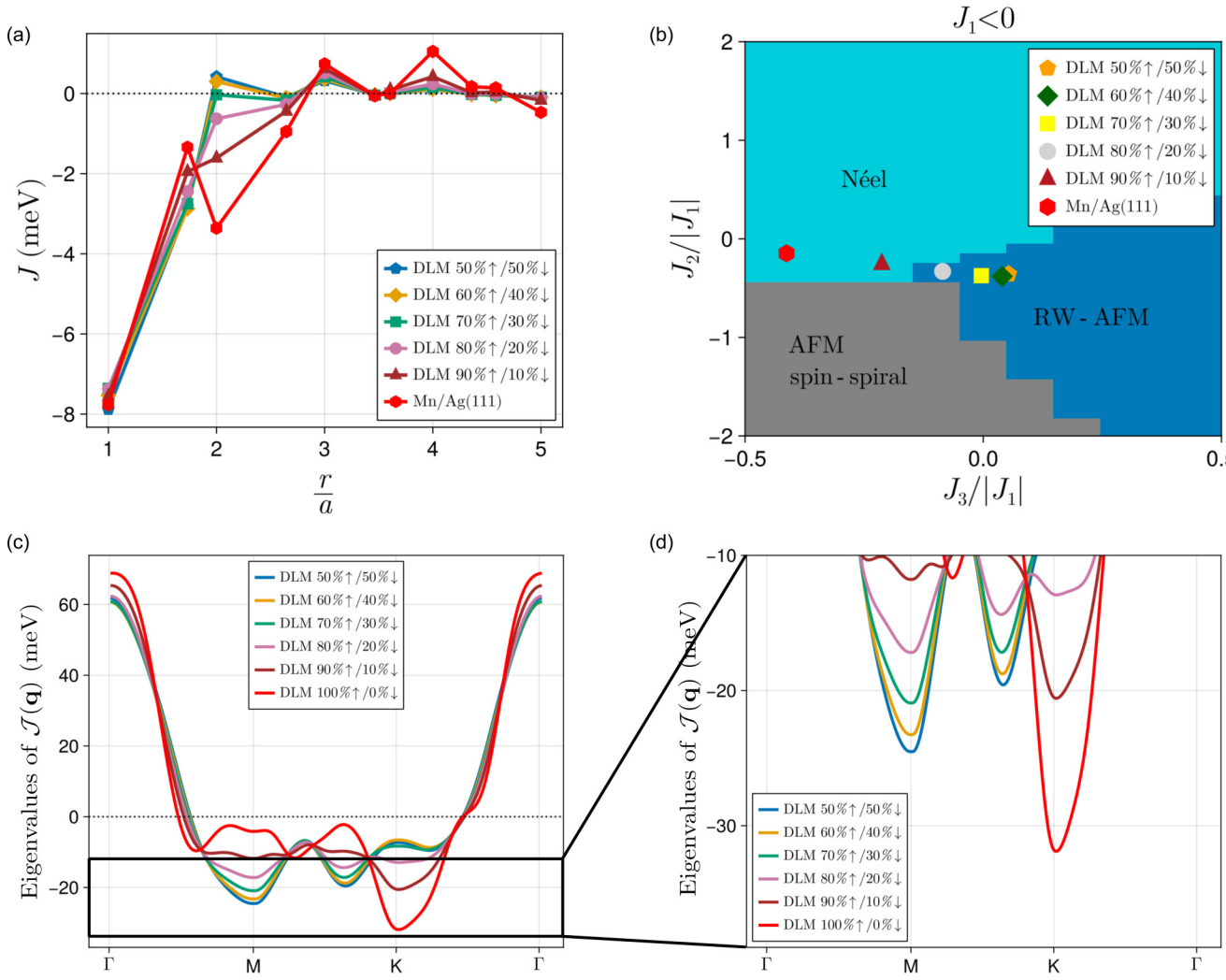

FIG. 6. (a)–(d) All results refer to fcc-stacked Mn on Ag(111) (a) Heisenberg exchange interactions as a function of distance for different DLM concentrations. (b) Phase diagram including the three nearest-neighbor (NN) interactions illustrating the impact of magnetic disorder on the ground state. (c) Eigenvalues of the Fourier-transformed exchange interactions along the high-symmetry path $\Gamma \rightarrow M \rightarrow K \rightarrow \Gamma$. The lowest values indicate the ground state.

Utilizing the all-electron KKR Green's function method, we find that the Mn monolayer, whether stacked on fcc or hcp sites, is characterized by a Néel magnetic state in full agreement with experimental observations. Our predictions indicate that this noncollinear magnetic state is in-plane and stacking-dependent chiral. The ground state chirality is dictated by the DMI, induced by the broken inversion symmetry at the interface and the spin-orbit coupling of the heavy Ag atoms, in combination with an in-plane MAE. Notably, the sense of chirality differs between the two stacking configurations due to their inverted structural symmetry.

We analyzed our results in terms of extracted magnetic interactions and the electronic structure. Interestingly, small variations in the exchange interactions—particularly the second- and third-nearest neighbors—are sufficient to switch the ground state between the Néel and the RW-AFM state. This explains the discrepancies in previously reported *ab initio* results and demonstrates the system's sensitivity to computational details and external conditions.

Subsequently, we extended our study to investigate the impact of magnetic disorder using the DLM approach, which mimics the effect of temperature on the electronic structure and magnetic interactions. For both fcc and hcp stacking, the DLM analysis reveals similar trends: while the nearest-neighbor Heisenberg exchange and DMI remain nearly constant, the MAE is strongly reduced with increasing disorder, and the third-nearest-neighbor interaction J_3 changes sign. This leads to a temperature-driven transition from a chiral Néel state to a collinear RW-AFM state, as supported by phase diagrams and Fourier-transformed exchange spectra.

In conclusion, our study demonstrates that for both fcc- and hcp-stacked Mn/Ag(111), the Néel state is the energetically favored ground state at low temperatures, in agreement with SP-STM experiments. With increasing temperature (or magnetic disorder), the system undergoes a transition to a RW-AFM state, driven by the sign change of J_3 and the suppression of MAE. Moreover, the stacking type not only influences the quantitative values of the magnetic interactions but also determines the chirality of the ground state. These

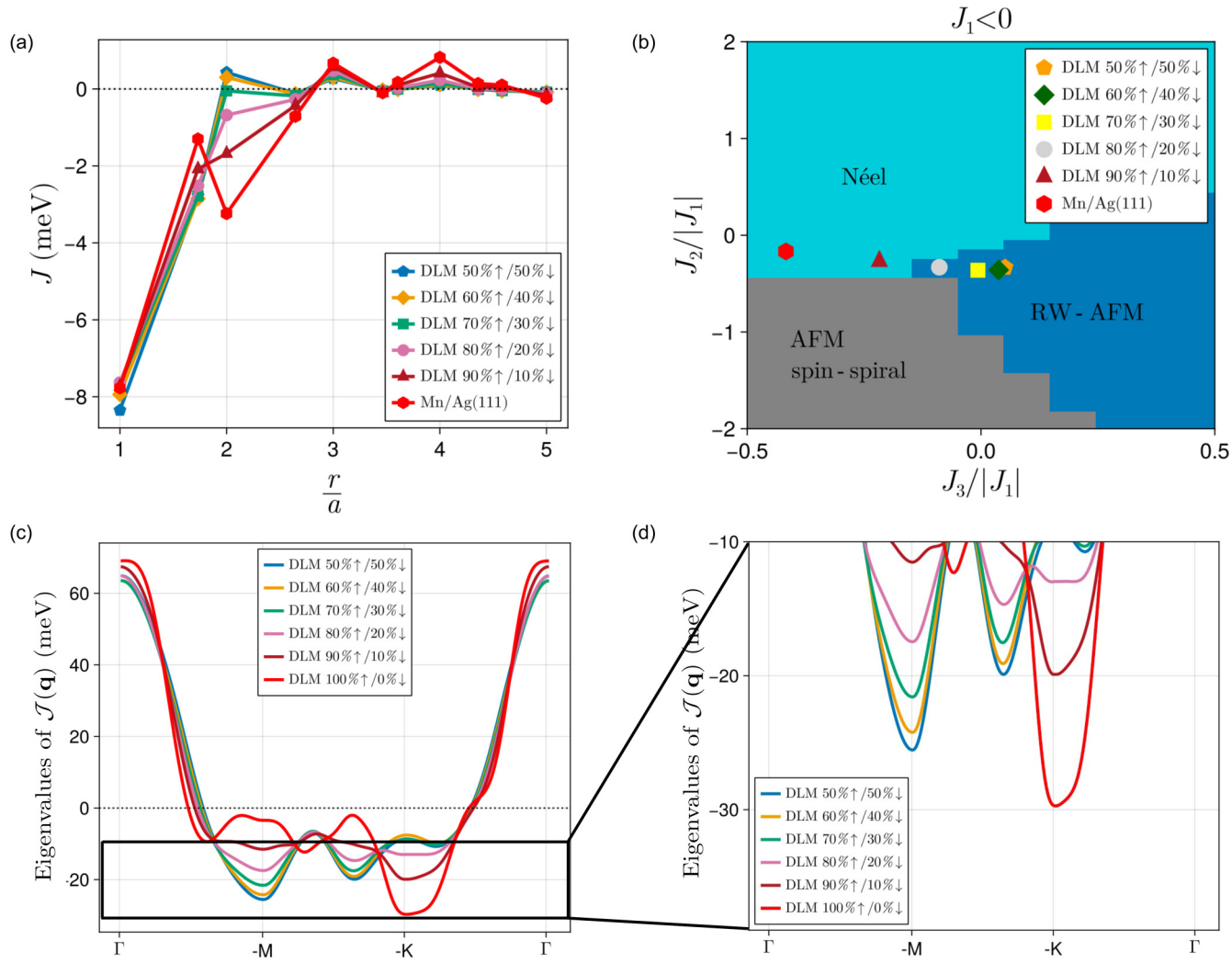

FIG. 7. (a)–(d) All results refer to hcp-stacked Mn on Ag(111) (a) Heisenberg exchange interactions as a function of distance for different DLM concentrations. (b) Phase diagram including the three NN interactions highlighting the influence of magnetic disorder on the ground state. (c) Eigenvalues of the Fourier-transformed exchange interactions along the reversed high-symmetry path $\Gamma \to -M \to -K \to \Gamma$. The lowest values indicate the ground state.

insights reconcile the contradictions in prior theoretical and experimental studies and highlight the role of stacking and temperature in stabilizing competing magnetic orders.

ACKNOWLEDGMENTS

We acknowledge fruitful discussions with Hangyu Zhou, Manuel dos Santos Dias, Jens Wiebe, Lucas Schneider, Sergiy Mankovsky, and Gustav Bihlmayer. Funding has been provided by the Priority Programmes SPP 2137 "Skyrmionics" (Project LO 1659/8-1) of the Deutsche Forschungsgemeinschaft (DFG). Computations were performed with computing resources granted by RWTH Aachen University under Project No. p0020362. We also acknowledge funding from German Excellence Strategy – EXC 3112/1 – 533767171 (Center for Chiral Electronics).

DATA AVAILABILITY

The data supporting the findings of this study are available from the authors upon reasonable request.

APPENDIX A: MAGNETIC INTERACTIONS VIA THE INFINITESIMAL ROTATION METHOD

Magnetic exchange interactions can be extracted within multiple-scattering theory using the infinitesimal rotation method [24,25], later extended to include spin-orbit-induced interactions [25,35]. This approach maps the second-order variation of the total energy, obtained from DFT, onto infinitesimal rotations of magnetic moments, providing direct access to the exchange interaction tensor.

According to the magnetic force theorem [36], the change in total energy upon infinitesimal rotation of magnetic moments simplifies to a change in single-particle energies:

$$\delta\mathcal{E} = \int_{-\infty}^{E_F} (E - E_F)\delta n(E) dE = -\int_{-\infty}^{E_F} \delta\mathcal{N}(E) dE, \quad \text{(A1)}$$

where $n(E) = \frac{d\mathcal{N}}{dE}$ is the density of states, $\mathcal{N}(E)$ the integrated density of states, and E_F the Fermi energy. Variations $\delta n(E)$,$\delta\mathcal{N}(E)$ arise from infinitesimal rotations from a reference collinear magnetic configuration.

TABLE I. Spin magnetic moments m, magnetic exchange interactions J, magnetic anisotropy energies (K) and Dzyaloshinskii-Moriya interaction (D) of the Mn monolayer fcc and hcp stacked on Ag(111) surface. The energy differences between the RW-AFM and the two chiral Néel states 1 [Fig. 5(a)] and 2 [Fig. 5(b)] are listed as obtained with spirit, with negative values indicating that the Néel state is lower energetically.

		100%	90%	80%	70%	60%	50%
fcc-Mn/Ag(111)	m (μ_B)	4.07	4.06	4.04	4.03	4.02	4.03
	K (meV)	−0.13	−0.05	−0.02	0.00	−0.01	0.01
	J_1 (meV)	−7.68	−7.56	−7.38	−7.36	−7.53	−7.88
	J_2 (meV)	−1.13	−1.95	−2.44	−2.75	−2.87	−2.82
	J_3 (meV)	−3.17	−1.61	−0.63	−0.03	0.30	0.42
	$\lvert\mathbf{D}_1\rvert$ (meV)	0.22	0.17	0.15	0.14	0.16	0.19
	$\lvert\mathbf{D}_2\rvert$ (meV)	0.03	0.01	0.00	0.02	0.05	0.07
	$\lvert\mathbf{D}_3\rvert$ (meV)	0.07	0.04	0.02	0.01	0.00	0.01
	$\Delta E_{\text{Néel1-RW-AFM}}$ (meV)	−27.50	−8.79	4.24	12.61	16.69	17.22
	$\Delta E_{\text{Néel2-RW-AFM}}$ (meV)	−26.55	−9.40	3.95	12.49	16.69	17.35
hcp-Mn/Ag(111)	m (μ_B)	4.07	4.06	4.05	4.03	4.03	4.04
	K (meV)	−0.10	−0.05	−0.01	0.01	0.02	0.02
	J_1 (meV)	−7.77	−7.73	−7.63	−7.69	−7.94	−8.35
	J_2 (meV)	−1.30	−2.08	−2.52	−2.78	−2.85	−2.78
	J_3 (meV)	−3.24	−1.68	−0.68	−0.05	0.30	0.43
	$\lvert\mathbf{D}_1\rvert$ (meV)	0.24	0.19	0.17	0.16	0.18	0.21
	$\lvert\mathbf{D}_2\rvert$ (meV)	0.03	0.01	0.00	0.02	0.05	0.08
	$\lvert\mathbf{D}_3\rvert$ (meV)	0.06	0.04	0.03	0.01	0.00	0.02
	$\Delta E_{\text{Néel1-RW-AFM}}$ (meV)	−25.48	−9.02	4.08	12.53	16.48	16.84
	$\Delta E_{\text{Néel2-RW-AFM}}$ (meV)	−26.30	−8.38	4.50	12.81	16.66	16.90

Using Lloyd's formula [37], the energy variation can be recast in terms of the scattering T matrix:

$$\delta\mathcal{E} = -\frac{1}{\pi}\int_{-\infty}^{E_F} \mathrm{Im\,Tr\,ln}\, T(E)dE, \tag{A2}$$

where the trace runs over site, orbital, and spin indices. The inverse T-matrix variation reads

$$(\delta T^{-1})^{ij}_{\alpha\sigma,\beta\sigma'} = (\delta t^{-1})^{i}_{\alpha\sigma\sigma'}\delta_{ij} - G^{\alpha\sigma,\beta\sigma'}_{ij}, \tag{A3}$$

with G_{ij} the structural Green's function and t the single-site scattering matrix.

The pairwise exchange interaction tensor $\mathcal{J}_{ij}$ is extracted from the second-order energy change due to infinitesimal rotations at sites i and j:

$$\delta\mathcal{E}_{ij} = -\delta\mathbf{S}_i^{\top}\cdot\mathcal{J}_{ij}\cdot\delta\mathbf{S}_j, \tag{A4}$$

where $\mathbf{S}_i$ denotes the unit vector of the local moment $\mathbf{m}_i$ at site i. The tensor components are

$$\mathcal{J}^{\alpha\beta}_{ij} = \frac{1}{2\pi}\int \mathrm{Im\,Tr}\left[\delta t_i^{\alpha} G_{ij}\delta t_j^{\beta} G_{ji}\right]dE, \tag{A5}$$

with $\delta t_i^{\alpha} = \frac{\partial t_i}{\partial S_i^{\alpha}}$ and $\delta t_i = \sum_{\alpha}\delta t_i^{\alpha}\delta S_i^{\alpha}$.

The variation δt_i^{α} is related to the exchange potential $B_i(r)$ defined in the local spin frame of reference of atom i via $\delta t_i^{\alpha} = \int dr\, R^{\top}(r)\sigma^{\alpha}B(r)R(r)$, where $R^{\top}(r)$ and $R(r)$ are, respectively, the left and right scattering solutions of the Dirac or Schrödinger equation including spin-orbit coupling [38], and σ^{α} are the Pauli matrices.

The exchange tensor $\mathcal{J}_{ij}$ is decomposed into isotropic, symmetric traceless, and antisymmetric components:

$$\mathcal{J}_{ij} = J_{ij}\mathbb{I} + \mathcal{J}^{\mathrm{S}}_{ij} + \mathcal{J}^{\mathrm{A}}_{ij}, \tag{A6}$$

with $J_{ij} = \frac{1}{3}\mathrm{Tr}(\mathcal{J}_{ij})$,

$$\mathcal{J}^{\mathrm{S}}_{ij} = \tfrac{1}{2}\left(\mathcal{J}_{ij} + \mathcal{J}_{ij}^{\top}\right) - J_{ij}\mathbb{I}, \tag{A7}$$

$$\mathcal{J}^{\mathrm{A}}_{ij} = \tfrac{1}{2}\left(\mathcal{J}_{ij} - \mathcal{J}_{ij}^{\top}\right). \tag{A8}$$

The antisymmetric part relates to the Dzyaloshinskii-Moriya vector $\mathbf{D}$ via

$$\mathcal{J}^{\mathrm{A}}_{ij} = \begin{pmatrix} 0 & D_z & -D_y \\ -D_z & 0 & D_x \\ D_y & -D_x & 0 \end{pmatrix}. \tag{A9}$$

When proceeding to the infinitesimal rotation of the magnetic moments, only certain components of $\mathcal{J}_{ij}$ are accessible given the initial magnetic moment direction. For instance:

(1) $\mathbf{m} \parallel x$: accessible yz block,

$$\mathcal{J}_{ij} = \begin{pmatrix} ? & ? & ? \\ ? & \mathcal{J}^{yy}_{ij} & \mathcal{J}^{yz}_{ij} \\ ? & \mathcal{J}^{zy}_{ij} & \mathcal{J}^{zz}_{ij} \end{pmatrix};$$

(2) $\mathbf{m} \parallel y$: accessible xz block,

$$\mathcal{J}_{ij} = \begin{pmatrix} \mathcal{J}^{xx}_{ij} & ? & \mathcal{J}^{xz}_{ij} \\ ? & ? & ? \\ \mathcal{J}^{zx}_{ij} & ? & \mathcal{J}^{zz}_{ij} \end{pmatrix};$$

(3) $\mathbf{m} \parallel z$: accessible xy block,

$$\mathcal{J}_{ij} = \begin{pmatrix} \mathcal{J}^{xx}_{ij} & \mathcal{J}^{xy}_{ij} & ? \\ \mathcal{J}^{yx}_{ij} & \mathcal{J}^{yy}_{ij} & ? \\ ? & ? & ? \end{pmatrix}.$$

Therefore, to extract the elements of the tensor of exchange interactions, the magnetic moments are rotated in the three directions, x, y, and z.

APPENDIX B: MAGNETIC INTERACTION FROM THE DLM METHOD

In the DLM method, the material is treated as a substitutional binary alloy within CPA. Each lattice site is occupied either by an atom with its magnetic moment aligned along a given direction, say the z axis, in the $\uparrow$ direction, with concentration $p_\uparrow$, or in the opposite direction ($\downarrow$), with concentration $p_\downarrow = 1 - p_\uparrow$.

The $\uparrow$ and $\downarrow$ atoms are introduced at site i in the effective CPA medium through defect matrices $X_{i\mu}$ ($\mu = \uparrow, \downarrow$) [39]. The effective CPA medium is characterized by the structural Green's function G_{ij}^{CPA}, which enters the infinitesimal rotation formulation of the exchange interactions via

$$\tilde{G}_{i\mu,j\nu} = X_{i\mu} G_{ij}^{\mathrm{CPA}} X_{j\nu}. \tag{B1}$$

This leads to the following expression for the components of the tensor of magnetic exchange interaction tensor:

$$\left(\mathcal{J}_{i\mu,j\nu}\right)^{\alpha\beta} = \frac{1}{2\pi} \int \mathrm{Im}\,\mathrm{Tr}\left[\delta t_{i\mu}^{\alpha} \tilde{G}_{i\mu,j\nu} \delta t_{j\nu}^{\beta} \tilde{G}_{j\nu,i\mu}\right] dE. \tag{B2}$$

Here, $\delta t_{i\mu}^{\alpha}$ denotes the variation of the single-site scattering matrix with respect to the α component of the local moment orientation at site i with configuration μ.

[1] S. Nakatsuji, N. Kiyohara, and T. Higo, Large anomalous Hall effect in a non-collinear antiferromagnet at room temperature, Nature (London) **534**, S5 (2016).

[2] Y. Takeuchi, Y. Yamane, J. Yoon, R. Itoh, B. Jinnai, S. Kanai, J. Ieda, S. Fukami, and H. Ohno, Chiral-spin rotation of non-collinear antiferromagnet by spin–orbit torque, Nat. Mater. **20**, 1364 (2021).

[3] A. Aldarawsheh, M. Sallermann, M. Abusaa, and S. Lounis, Intrinsic Néel antiferromagnetic multimeronic spin textures in ultrathin films, J. Phys. Chem. Lett. **14**, 8970 (2023).

[4] A. Aldarawsheh, M. Sallermann, M. Abusaa, and S. Lounis, A spin model for intrinsic antiferromagnetic skyrmions on a triangular lattice, Front. Phys. **11**, 1175317 (2023).

[5] N. Abuawwad, M. dos Santos Dias, H. Abusara, and S. Lounis, $CrTe_2$ As a two-dimensional material for topological magnetism in complex heterobilayers, Phys. Rev. B **108**, 094409 (2023).

[6] L. Balents, Spin liquids in frustrated magnets, Nature (London) **464**, 199 (2010).

[7] B. Rimmler, B. Pal, and S. S. P. Parkin, Non-collinear antiferromagnetic spintronics, Nat. Rev. Mater. **10**, 109 (2024).

[8] P. Kurz, Non-collinear magnetism at surfaces and in ultrathin films, Ph.D. dissertation, RWTH-Aachen University, 2000.

[9] S. Heinze, P. Kurz, D. Wortmann, G. Bihlmayer, and S. Blügel, Complex magnetism in ultra-thin films: Atomic-scale spin structures and resolution by the spin-polarized scanning tunneling microscope, Appl. Phys. A **75**, 25 (2002).

[10] B. Malonda-Boungou, S. Meza-Aguilar, A. Debernardi, and A. Raji, Non-collinear magnetism in Mn monolayer on Ag(111) fcc: Density functional calculations, Comput. Condens. Matter **19**, e00368 (2019).

[11] P. Krüger, M. Taguchi, and S. Meza-Aguilar, Magnetism of 3*d* transition-metal monolayers on Cu(111) and Ag(111), Phys. Rev. B **61**, 15277 (2000).

[12] M. dos Santos Dias, J. B. Staunton, A. Deak, and L. Szunyogh, Anisotropic spin-spin correlations in $Mn_1/X(111)$ (X = Pd, Pt, Ag, and Au), Phys. Rev. B **83**, 054435 (2011).

[13] C. L. Gao, W. Wulfhekel, and J. Kirschner, Revealing the 120° antiferromagnetic Néel structure in real space: One monolayer Mn on Ag(111), Phys. Rev. Lett. **101**, 267205 (2008).

[14] A. Rodríguez-Sota, V. Saxena, J. Spethmann, R. Wiesendanger, R. Lo Conte, A. Kubetzka, and K. von Bergmann, Phase coexistence of Mn trimer clusters and antiferromagnetic Mn islands on Ir(111), ACS Nano **18**, 3699 (2024).

[15] A. Dal Corso, Pseudopotentials periodic table: From H to Pu, Comput. Mater. Sci. **95**, 337 (2014).

[16] P. Giannozzi, *et al.*, QUANTUM ESPRESSO: a modular and open-source software project for quantum simulations of materials, J. Phys.: Condens. Matter **21**, 395502 (2009).

[17] P. Rüßmann, *et al.*, JuDFTteam/JuKKR: v3.6, Zenodo (2022), https://doi.org/10.5281/zenodo.7284739.

[18] B. L. Gyorffy, A. J. Pindor, J. Staunton, G. M. Stocks, and H. Winter, A first-principles theory of ferromagnetic phase transitions in metals, J. Phys. F **15**, 1337 (1985).

[19] J. B. Staunton and B. L. Gyorffy, Onsager cavity fields in itinerant-electron paramagnets, Phys. Rev. Lett. **69**, 371 (1992).

[20] J. B. Staunton, L. Szunyogh, A. Buruzs, B. L. Gyorffy, S. Ostanin, and L. Udvardi, Temperature dependence of magnetic anisotropy: An *ab initio* approach, Phys. Rev. B **74**, 144411 (2006).

[21] S. Vosko, L. Wilk, and M. Nusair, Accurate spin-dependent electron liquid correlation energies for local spin density calculations: a critical analysis, Can. J. Phys. **58**, 1200 (1980).

[22] I. Dzyaloshinsky, A thermodynamic theory of "weak" ferromagnetism of antiferromagnetics, J. Phys. Chem. Solids **4**, 241 (1958).

[23] T. Moriya, Anisotropic superexchange interaction and weak ferromagnetism, Phys. Rev. **120**, 91 (1960).

[24] A. Liechtenstein, M. Katsnelson, V. Antropov, and V. Gubanov, Local spin density functional approach to the theory of exchange interactions in ferromagnetic metals and alloys, J. Magn. Magn. Mater. **67**, 65 (1987).

[25] H. Ebert and S. Mankovsky, Anisotropic exchange coupling in diluted magnetic semiconductors: *Ab initio* spin-density functional theory, Phys. Rev. B **79**, 045209 (2009).

[26] T. Hatanaka, J. Bouaziz, T. Nomoto, and R. Arita, Calculation of the biquadratic spin interactions based on the spin cluster expansion for *ab initio* tight-binding models, J. Phys. Soc. Jpn. **94**, 124709 (2025).

[27] D. Böttcher, A. Ernst, and J. Henk, Temperature-dependent Heisenberg exchange coupling constants from linking electronic-structure calculations and Monte Carlo simulations, J. Magn. Magn. Mater. **324**, 610 (2012).

[28] L. Szunyogh, L. Udvardi, J. Jackson, U. Nowak, and R. Chantrell, Atomistic spin model based on a spin-cluster expansion technique: Application to the $IrMn_3$/Co interface, Phys. Rev. B **83**, 024401 (2011).

[29] G. P. Müller, M. Hoffmann, C. Dißelkamp, D. Schurhoff, S. Mavros, M. Sallermann, N. S. Kiselev, H. Jonsson, and S. Blugel, Phys. Rev. B **99**, 224414 (2019).
[30] The spirit code can be found at https://juspin.de.
[31] J. Spethmann, S. Meyer, K. von Bergmann, R. Wiesendanger, S. Heinze, and A. Kubetzka, Discovery of magnetic single- and triple-**q** states in Mn/Re(0001), Phys. Rev. Lett. **124**, 227203 (2020).
[32] A. Aldarawsheh, I. L. Fernandes, S. Brinker, M. Sallermann, M. Abusaa, S. Blügel, and S. Lounis, Emergence of zero-field non-synthetic single and interchained antiferromagnetic skyrmions in thin films, Nat. Commun. **13**, 7369 (2022).
[33] A. Fert and P. M. Levy, Role of anisotropic exchange interactions in determining the properties of spin-glasses, Phys. Rev. Lett. **44**, 1538 (1980).
[34] E. Mendive-Tapia, M. dos Santos Dias, S. Grytsiuk, J. B. Staunton, S. Blügel, and S. Lounis, Short period magnetization texture of B20-MnGe explained by thermally fluctuating local moments, Phys. Rev. B **103**, 024410 (2021).
[35] L. Udvardi, L. Szunyogh, K. Palotás, and P. Weinberger, First-principles relativistic study of spin waves in thin magnetic films, Phys. Rev. B **68**, 104436 (2003).
[36] A. Oswald, R. Zeller, P. J. Braspenning, and P. H. Dederichs, Interaction of magnetic impurities in Cu and Ag, J. Phys. F **15**, 193 (1985).
[37] P. Lloyd and P. V. Smith, Multiple scattering theory in condensed materials, Adv. Phys. **16**, 67 (1967).
[38] D. S. G. Bauer, Development of a relativistic full-potential first-principles multiple scattering green function method applied to complex magnetic textures of nano structures at surfaces, Ph.D. thesis, Jülich, 2013.
[39] Introduction, in *Electron Scattering in Solid Matter*, edited by J. Zabloudil, R. Hammerling, P. Weinberger, and L. Szunyogh (Springer, Berlin, Heidelberg, 2005), pp. 1–4.